Spherical Harmonics and Discontinuous Galerkin Finite Element Methods for the Three-Dimensional Neutron Transport Equation: Application to Core and Lattice Calculation

Kenneth Assogba, Lahbib Bourhrara, Igor Zmijarevic, Grégoire Allaire, Antonio Galia

Spherical Harmonics and Discontinuous Galerkin Finite Element Methods for the Three Dimensional Neutron Transport Equation: Application to Core and Lattice Calculation

Kenneth Assogba*, Lahbib Bourhrara*, Igor Zmijarevic*, Grégoire Allaire†, Antonio Galia*

Abstract

The spherical harmonics or P_N method is intended to approximate the neutron angular flux by a linear combination of spherical harmonics of degree at most N. In this work, the P_N method is combined with discontinuous Galerkin finite elements method and yield to a full discretization of the multigroup neutron transport equation. The employed method is able to handle all geometries describing the fuel elements without any simplification nor homogenisation. Moreover the use of a matrix assembly-free method avoids building large sparse matrices, which enables to produce high-order solutions in small computational time and less storage usage. The resulting transport solver called `NYMO` has a wide range of applications: it can be used for a core calculation as well as for a precise 281-groups lattice calculation accounting anisotropic scattering. To assess the accuracy of this numerical scheme, it was applied to 3D reactor core and fuel assembly calculations. These calculations point out that the proposed P_N-DG method is capable of producing precise solutions while the developed solver is able to handle complex 3D core and assemblies geometries.

Keywords— discontinuous Galerkin FEM, spherical harmonics method, neutron transport equation, unstructured meshes, non-conforming meshes

1 Introduction

Deterministic solutions of Boltzmann transport equation on unstructured and non-conforming meshes are in high demand in the industry for the past few years due to the rapid development of advanced nuclear reactor concepts and high-performance computing clusters. In this work we combine spherical harmonics and discontinuous Galerkin methods to obtain a complete discretization of the multigroup neutron transport problem [10] defined on the phase space $X = D \times \mathbf{S}^2 \ni (x, \omega)$. The unit sphere $\mathbf{S}^2$ is the angular domain and the reactor domain D is a bounded set of $\mathbb{R}^d$ where $d = 1, 2$ or 3. We are particularly interested in the study of three-dimensional configurations.

The P_N method [8] consists in approximating the angular neutron flux $u(x, \omega)$ by the truncated series over $y_n^m(\omega)$ the real spherical harmonics [16, Appendix A]

$$u(x, \omega) \approx \sum_{n=0}^{N} \sum_{m=-n}^{n} u_n^m(x) y_n^m(\omega). \tag{1}$$

The well established discrete ordinates or S_N method [6] is known to suffer from nonphysical oscillations, also referred as ray effects [13]: in a medium with little or no scattering a source is propagated preferentially along the ordinate directions, leading to artificially non-monotoneous flux behavior. Since the angular flux is approximated for all direction, P_N method is immune to ray effects. However in the past, P_N discretization had the reputation of being difficult to implement and memory intensive in two and three dimension. To overcome these challenges, the P_N community has been continuously improving its methods and codes, leading to advanced transport solvers. One can cite the `EVENT` code [9], the Argonne National Laboratory nodal transport solver `VARIANT` [15]

*Université Paris-Saclay, CEA, Service d'Études des Réacteurs et de Mathématiques Appliquées, 91191 Gif-sur-Yvette, France (kenneth.assogba@cea.fr, lahbib.bourhrara@cea.fr, igor.zmijarevic@cea.fr, antonio.galia@cea.fr)

†CMAP, École polytechnique, Institut Polytechnique de Paris, 91120 Palaiseau, France (gregoire.allaire@polytechnique.fr)

and the domain decomposition based solver PARAFISH [28]. However, these solvers are limited to meshes with straight edges and faces. The ability for a spatial approximation to handle curved shaped elements allows for an exact representation of the annular sectors, typical of a fuel pellet.

In this work, the remain spatial unknown, called angular flux moments $u_n^m(x)$ from (1) are approximated using discontinuous Galerkin (DG) finite element method. Introduced by Reed and Hill [21] in the early 70s, DG method is well suited for hyperbolic problems. In addition DG provide the flexibility to handle non-conforming and unstructured meshes and the small stencil renders the DG methods extremely parallelizable. One can argue to finish that DG achieve with ease high-order accuracy. Assuming the flux moment $u_n^m(x)$ polynomial of degree at most k leads to a $k + \frac{1}{2}$ order of convergence [12].

Based on the variational formulation proposed in [3], a new approximation method for the Boltzmann transport equation is presented in [4]. The resulting solver called NYMO has been implemented in the frame of CEA reactor physics platform APOLLO3 ® [23]. The proposed numerical method can treat 2D unstructured and non-conforming meshes with line segments, circles and circular arcs [26]. Hence heterogeneous pin-cell geometries with concentric annular regions can be modeled without any approximation. We use matrix assembly-free technique to leverage the common concern about memory usage, thus high-order approximation can be considered. The code is written in C++ and compute-intensive tasks like matrix-vector product operators are parallelized using OpenMP.

First results for 3D reactor core k-eigenvalue calculation have been shown in [1]. The purpose of this paper is to present extension of the NYMO capabilities to 3D prismatic meshes, Figure 1. The novelty here is the versatile use of this solver to efficiently perform 3D reactor core and fuel assemblies calculations.

This paper is organized as follows. In section 2 we recast the neutron transport problem into an equivalent variational formulation. Then the angle-space approximation framework is introduced in section 3. In particular, we describe the calculation of the coefficients of the elementary matrices in 3D, and the method for solving the linear system resulting from the discretization without assembly. Section 4 finally presents applications of the P_N-DG discretization on core and lattice calculation with various geometries and optical properties.

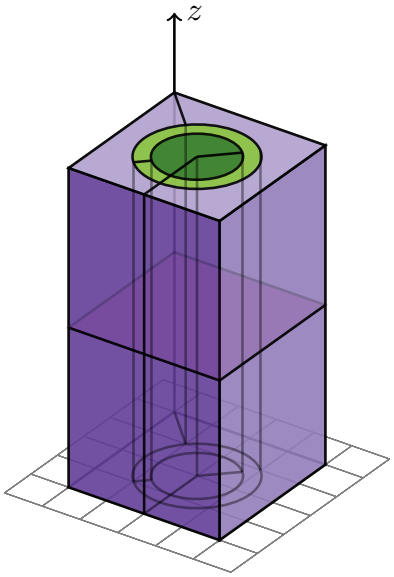

Figure 1: An example of a 3D fuel-cell mesh supported by NYMO. In 2D NYMO supports non-conforming unstructured meshes with curved elements. In 3D it supports 2D extruded meshes.

2 The continuous problem

The steady-state linear Boltzmann equation models the behavior of neutral particle population subjected to diverse interactions with matter: absorption, collisions, fission, at any point of the space-angle-energy phase space. The multigroup discretization [16] allows to pass from continuous energy to an approximation by a finite number G of energy groups. The number of energy groups varies between 2 (fast and slow neutrons) and 281 for a fine control over energy variations during a typical pressurized water reactor lattice calculation. In the rest of this section we introduce the notations used, the transport problem studied and present the variational formulation.

2.1 Neutron transport problem

Let us consider $x \in D$ with D an open bounded set in $\mathbf{R}^d$ ($d = 1$, 2 or 3), with boundary ∂D and outward normal n. Let $\omega \in \mathbf{S}^2$ with $\mathbf{S}^2$ the unit sphere of $\mathbf{R}^3$. The angular domain $\mathbf{S}^2$ is parametrized by two angles $\theta \in [0, \pi]$ and $\varphi \in [0, 2\pi]$ such that $\omega(\theta, \varphi) \in \mathbf{S}^2$, $\omega_x = \sin\theta\cos\varphi$, $\omega_y = \sin\theta\sin\varphi$ and $\omega_z = \cos\theta$. The integral over $\mathbf{S}^2$ is defined by

$$\int_{\mathbf{S}^2} f(\omega)d\omega = \frac{1}{4\pi}\int_0^{2\pi}\left(\int_0^{\pi} f(\theta,\varphi)\sin\theta d\theta\right)d\varphi.$$

The integer g identifies the energy group and $g \in [\![1, G]\!]$. The multigroup flux is then denoted $u = (u^g(x,\omega))_{g=1,\cdots,G}$.

Let us define the scattering operator H, modeling the transfer of neutrons from an energy-group g' to another group g after collision

$$(H^g u)(x,\omega) = \sum_{g'=1}^{G}\int_{\mathbf{S}^2}\sigma_s^{g,g'}(x,\omega\cdot\omega')u^{g'}(x,\omega')d\omega', \tag{2}$$

with $\sigma_s^{g,g'}$ being the transfer cross-section, generally anisotropic.

The fission operator F is defined as

$$(F^g)(x,\omega) = \sum_{\alpha}\chi_\alpha^g(x)\sum_{g'=1}^{G}\nu\sigma_{f,\alpha}^{g'}(x)\int_{\mathbf{S}^2}u^{g'}(x,\omega')d\omega'. \tag{3}$$

The quantities $\nu\sigma_{f,\alpha}^g$ and χ_α^g are respectively the fission production rate and the fission emission spectrum for isotope α. The sum over α represent the sum over fissile isotopes.

Given an external source $q = (q^g)_{g=1,\cdots,G}$, an incoming flux $f = (f^g)_{g=1,\cdots,G}$ through the inflow boundary Γ_-, and the different neutron cross-sections, we seek the multigroup flux $(u^g(x,\omega))_{g=1,\cdots,G}$ and eventually the associated eigenvalue λ solution of

$$\omega\cdot\nabla u^g + \sigma^g u^g = H^g u + \frac{1}{\lambda}F^g u + q^g \quad \text{in } X = D\times\mathbf{S}^2, \tag{4}$$

with the boundary condition

$$u^g = f^g \quad \text{on } \Gamma_-, \tag{5}$$

where σ^g is the total cross-section and $\Gamma_\pm = \{(x,\omega)\in\partial D\times\mathbf{S}^2,\ \pm\omega\cdot n(x) > 0\}$.

In absence of external source and incoming flux, that is q and f are zero, equation (4) is studied as an eigenvalue problem, the objective being to obtain the effective multiplication factor $k_{eff} = \lambda$. In the other cases, one sets $\lambda = 1$ and one refers to a source problem.

2.2 Variational formulation

From here on, σ^g the total cross section is assumed to be a positive non-vanishing function. The variational formulation proposed in [3] consists in multiplying (4) by the term $v + \frac{1}{\sigma}(\omega\cdot\nabla v)$, with v a sufficiently smooth test function. The variational space used is the space W where lives the unique solution of the transport problem [7]

$$W = \left\{v \in L^2(X)\ /\ \omega\cdot\nabla v \in L^2(X),\ v|_{\Gamma_+}\in L^2(\Gamma_+, |\omega\cdot n|dsd\omega)\right\}. \tag{6}$$

For all groups $g = 1,\cdots,G$, the variational problem obtained reads,

$$\text{find } u\in W \ \text{ such that } \ a^g(u^g,v) = h^g(u,v) + \frac{1}{\lambda}p^g(u,v) + L^g(v),\ \ \forall v\in W \tag{7}$$

with

$$a^g(u^g,v) = \int_X\left(\frac{1}{\sigma^g}(\omega\cdot\nabla u^g)(\omega\cdot\nabla v) + \sigma^g u^g v\right)d\omega dx + \int_{\Gamma_+}u^g v(\omega\cdot n)d\omega ds, \tag{8}$$

$$h^g(u,v) = \int_X\left((H^g u)v + \frac{1}{\sigma^g}(H^g u)(\omega\cdot\nabla v)\right)d\omega dx, \tag{9}$$

$$p^g(u,v) = \int_X\left((F^g u)v + \frac{1}{\sigma^g}(F^g u)(\omega\cdot\nabla v)\right)d\omega dx, \tag{10}$$

$$L^g(v) = \int_X\left(q^g v + \frac{1}{\sigma^g}q^g(\omega\cdot\nabla v)\right)d\omega dx - \int_{\Gamma_-}f^g v(\omega\cdot n)d\omega ds. \tag{11}$$

Under reasonable assumptions about the problem data, it has been established in [3] that the variational formulation (7) is equivalent to the original transport problem (4). Equivalence of this formulation with transport self-adjoint angular flux equation (SAAF) [20], least-squares approach and the even (or odd) parity formulation [16, §6] is discussed in [4, §3].

Since σ^g is assumed to be non-zero, fully voided regions cannot be modeled. However, numerical tests show that almost voided regions, with σ of the order of 10^{-6} are supported.

3 Phase space discretization

The numerical scheme used to solve problem (7) combines spherical harmonics method for the treatment of angular dependence and discontinuous Galerkin finite element method for spatial discretization. The link between mesh regions is done using upwind flux at cell interfaces. From [5] we know that DG discretization of the linear advection equation based on upwind flux is stable. From here on, the energy group number g will be omitted if not needed.

3.1 Angular discretization

The neutron angular flux $u(x,\omega)$ can be expanded exactly in terms of real-valued spherical harmonics functions $y_n^m(\omega)$ [16, Appendix A]

$$u(x,\omega) = \sum_{n=0}^{\infty} \sum_{m=-n}^{n} (u, y_n^m)_{\mathbf{S}^2} y_n^m(\omega),$$

where $(\cdot,\cdot)_{\mathbf{S}^2}$ denotes the inner product of $L^2(\mathbf{S}^2)$. Introducing the angular flux moments $u_n^m(x) = (u, y_n^m)_{\mathbf{S}^2}$ we then write

$$u(x,\omega) = \sum_{n=0}^{\infty} \sum_{m=-n}^{n} u_n^m(x) y_n^m(\omega) \tag{12}$$

The first $u_0^0(x)$ and second $(u_1^m(x))_{m\in\{-1,0,1\}}$ angular moments of u are respectively the scalar flux and current vector. The $\mathrm{P_N}$ method consists in truncating the expansion (12) of the angular flux to the order N, that is:

$$u(x,\omega) \approx u_N(x,\omega) = \sum_{n=0}^{N} \sum_{m=-n}^{n} u_n^m(x) y_n^m(\omega), \tag{13}$$

It remains to determine the flux moments $u_n^m(x)$.

3.2 Spatial discretization

We proceed to the spatial discretization using DG finite elements.

3.2.1 Three-dimensional meshes

The spatial domain D is meshed into disjoints elements (or regions) D_r. The mesh can be unstructured and non-conforming, that is with hanging nodes. Curved elements (circle or circular arc) are considered to be able to represent cladding surrounding the fuel rods. In 3D, prismatic meshes are sufficient to model the geometry of most types of nuclear reactors. Then each 3D region D_r^{3D} is given as a base face D_r^{2D} extruded along the z direction:

$$D_r^{3D} = D_r^{2D} \times [z_0, z_1].$$

Each face F^{3D} of ∂D_r^{3D} is either a horizontal face or a vertical face. The vertical faces are obtained by extruding a line segment, circle or a circular arc in the horizontal plane along the z axis. Horizontal faces treatment is identical to that of 2D regions.

$$F^{3D} = \begin{cases} F^{2D} \times [z_0, z_1] \text{ if } F^{3D} \text{ is vertical,} \\ D_r^{2D} \times \{z_0\} \text{ else.} \end{cases}$$

3.2.2 Angular moments approximation

To obtain a full discretization, the angular flux moments $u_n^m(x)$ are approximated by piecewise polynomial over the mesh D_h of domain D. With any $D_r \in D_h$, we associate a finite-dimensional space $\mathbb{P}^k(D_r)$ of d-variate polynomials of total degree at most k on D_r. Then we collect all those spaces to form the space of piecewise polynomials over D_h

$$\mathbb{P}_h^k = \left\{ v \in L^2(D);\ \forall D_r \in D_h,\ v|_{D_r} \in \mathbb{P}^k(D_r) \right\}. \tag{14}$$

Given a basis, let say $\varphi_j(x)$ of $\mathbb{P}_h^k$, the fully discrete solution $u_{N,k}$ can be written as a weighted sum of basis functions $\varphi_j y_n^m$:

$$u_{N,k} = \sum_{n=0}^{N} \sum_{m=-n}^{n} \sum_{j=1}^{J} u_{n,j}^m \varphi_j(x) y_n^m(\omega), \tag{15}$$

Here J represent the total number of spatial degree of freedom. The coefficients $u_{n,j}^m$ fully determine the approximated flux. The incoming flux f and the source term q are approximated in the same way. The approximation space is

$$W_h = \operatorname{span}(\varphi_j y_n^m) \tag{16}$$

and it is useful to notice that

$$\dim W_h = \operatorname{card}(D_h) \binom{k+d}{d} (N+1)\left(\frac{d-1}{2}N + 1\right).$$

Taking into account the energy discretization for a multigroup calculation, the total number of degrees of freedom is $\#\text{dof} = G \dim W_h$.

The local approximation space $W_h(D_r)$ on each element is obtained using the space $\mathbb{P}^k(D_r)$ instead of the whole polynomial space $\mathbb{P}_h^k$. The table 1 provides the number of degrees of freedom per element induced by a $\mathrm{P_N}$-DG (P_N-$\mathbb{P}^k$) discretization in 3D.

Table 1: Number of degrees of freedom per element involved in a 3D $\mathrm{P_N}$-DG discretization.

#dof	P_0	P_1	P_2	P_3	P_4	P_5	P_6
$\mathbb{P}^0$	1	4	9	16	25	36	49
$\mathbb{P}^1$	4	16	36	64	100	144	226
$\mathbb{P}^2$	10	40	90	160	250	360	490

3.3 The fully discretized problem

Due to the discontinuous nature of the spatial approximation, a numerical flux at mesh cell interfaces have to be set. The natural choice when dealing with particle transport is the upwind numerical flux [21, 14]. For an interior face F shared by two cells D_{r1} and D_{r2} with respective outward normal n_1, n_2, the numerical flux across F is given by

$$\mathcal{F}(u) = u^{\uparrow} = \begin{cases} u|_{D_{r2}}, & \text{if } \omega \cdot n_1 < 0 \\ u|_{D_{r1}}, & \text{if } \omega \cdot n_1 > 0. \end{cases} \tag{17}$$

For $F \in \partial D$ a boundary face with outward normal n

$$\mathcal{F}(u) = \begin{cases} f, & \text{if } \omega \cdot n < 0 \\ u, & \text{if } \omega \cdot n > 0. \end{cases} \tag{18}$$

In particular, inside a region D_{r1} the incoming flux on a face $F \in \partial D_{r1}$ is given either by the boundary condition f if $F \in \partial D_{r1} \cap \partial D$ or by the flux in the adjacent region D_{r2} if F is an interface. Using this we derive a local variational formulation. On each mesh element D_r, let us denote by a_r, h_r and p_r the restriction of the bilinear forms defined in (8) - (10) to the local phase space $X_r = D_r \times \mathbf{S}^2$. For all cells $D_r \in D_h$ the local discretized problem reads,

$$\text{find } u \in W_h(D_r) \text{ such that } a_r(u,v) = h_r(u,v) + \frac{1}{\lambda} p_r(u,v) + L_r(v),\ \ \forall v \in W_h(D_r) \tag{19}$$

with

$$L_r(v) = \int_{X_r} \left(qv + \frac{1}{\sigma} q(\omega \cdot \nabla v) \right) d\omega dx - \int_{\Gamma_-(D_r)} \mathcal{F}(u) v (\omega \cdot n) d\omega ds. \tag{20}$$

Defined at (21), $\Gamma_-(D_r)$ denote the inflow boundary of X_r. Following definitions (17) and (18) one can notice that in (20), $\mathcal{F}(u)$ is independent of u, and is either the boundary flux f or the flux coming from the neighbouring regions of D_r.

Furthermore, one can sum (19) over all mesh elements to obtain a global formulation. In practice, the local formulation is the one used for implementation purpose, since as described in the section 3.5, the matrices resulting from the discretization are not assembled.

The standard finite element framework follows by replacing u, f and q by their respective approximations and v with $\varphi_{j'}(x) y_{n'}^{m'}(\omega)$ in (19). One obtains a matrix system of unknowns $u_{n,j}^m$ (15). The determination of these matrices therefore involves the calculation of volume integrals and surface integrals.

3.4 3D Elementary Matrices

Following the 3D mesh cells and faces classification presented in 3.2.1, one can notice that 3D matrix resulting from the discretization can be recasted into 2D matrix calculations. We refer to [4] for more details about 2D matrix calculation.

Three kinds of integrals are encountered after discretization: volumic integrals $\int_{D_r} \bullet dx$, integrals over the angular variable $\int_{\mathbf{S}^2} \bullet d\omega$ and integrals over the boundary of a region ($\Gamma_\pm(D_r)$) where the two types mentioned above are coupled $\int_{\partial D_r} \int_{\pm(\omega \cdot n)>0} \bullet (\omega \cdot n) d\omega ds$. The first two are straightforward to compute. We describe how to calculate the third integral type, depending on the type of face: horizontal or vertical.

A region boundary can be rewritten

$$\Gamma_\pm(D_r) = \bigcup_{F \in \partial D_r} \left\{ (x, \omega) \in F \times \mathbf{S}^2 \ / \ \pm \omega \cdot n_F > 0 \right\}. \tag{21}$$

Let us denote n the unit outgoing normal. The map from cartesian to spherical coordinates is $(n_x, n_y, n_z) \mapsto (\theta_n, \varphi_n)$ with $n_x = \sin\theta_n \cos\varphi_n$, $n_y = \sin\theta_n \sin\varphi_n$ and $n_z = \cos\theta_n$. The third integral type can then be rewritten using

$$\int_{\pm(\omega \cdot n)>0} y(\omega)(\omega \cdot n) d\omega = \int_{\theta_0}^{\theta_1} f(\theta) d\theta \int_{\varphi_0}^{\varphi_1} g(\varphi) d\varphi.$$

It remains to determine θ_0, θ_1, φ_0 and φ_1.

3.4.1 Horizontal faces

If the face F is a bottom base of D_r, then $n(0, 0, -1)$ and $\omega \cdot n = -\cos\theta$. On the incoming half-sphere $\mathbf{S}_-^2$, $\omega \cdot n < 0$ implies $-\cos(\theta) < 0$. Therefore $\theta \in \left[-\frac{\pi}{2}, \frac{\pi}{2}\right] \cap [0, \pi]$ and finally $\theta_0 = 0$ and $\theta_1 = \frac{\pi}{2}$. Symmetrically for the outgoing half-sphere $\mathbf{S}_+^2$, $\theta_0 = \frac{\pi}{2}$ and $\theta_1 = \pi$. In the two cases $\varphi_0 = 0$ and $\varphi_1 = 2\pi$. The same developments applies for upper horizontal faces.

3.4.2 Vertical faces

If the face F is a flat lateral face of D_r, using $\theta_n = \frac{\pi}{2}$ implies $n(\cos\varphi_n, \sin\varphi_n, 0)$ then $\omega \cdot n = \sin\theta \cos(\varphi - \varphi_n)$. Since $\theta \in [0, \pi]$, the sign of $\omega \cdot n$ only depends on the sign of $\cos(\varphi - \varphi_n)$. On the incoming half-sphere, $\omega \cdot n < 0$ implies $\varphi_0 = \varphi_n + \frac{\pi}{2}$ and $\varphi_1 = \varphi_n + 3\frac{\pi}{2}$. Symmetrical arguments applies for the outgoing half-sphere. In the two cases $\theta_0 = 0$ and $\theta_1 = \pi$. The case of curved lateral faces can also be treated by noting that the normal n in this case is parametrized by an element M of the arc at the base of the face. In summary $n = n(M)$ with $n_x = \cos(\varphi_n(M))$, $n_y = \sin(\varphi_n(M))$ and $n_z = 0$.

3.5 Assembly-free linear system resolution

Geometrically, a reactor core consists of a set of assemblies, similarly each assembly is made up of a set of fuel rods. One can therefore consider using these repetitive patterns to significantly reduce the memory footprint and the simulation time. Indeed, due to the choice of the basis functions $(\varphi_j)_j$, presented in [4, §13], from two mesh elements identical by translation, the same elementary matrices are produced. More precisely, we refer to geometric elementary matrices, as they do not depend on the cross-sections in the region. These elements can be grouped by clusters of elements identical up to a translation, thus defining an equivalence class, Figure 2. We

define the equivalence class $[D_r]$ of an element $D_r \in D_h$ as the set of cells $D_s \in D_h$ such that D_s is the image of D_r by a translation, let us note $D_s \sim D_r$

$$D_s \in [D_r] \Leftrightarrow D_s \sim D_r.$$

Two elements of the mesh D_h are equivalent to each other if and only if they belong to the same equivalence class. Any element of $[D_r]$ characterizes the class, and may be used to represent it. In practice the chosen representative is the cell with the smallest r number.

First, we need to determine the set of equivalence classes of the mesh, with respect to the equivalence relation $\sim$, called the quotient set. The underlying idea is to work in the quotient set as on the mesh, but without distinguishing between equivalent elements. It is therefore sufficient to calculate the geometric elementary matrices of each class representative. Likewise the matrix-vector product operator is written using the canonical application $D_r \mapsto D_r^\star$, which associates to each element of D_h its class representative. The reuse of data already present inside the cache memory reduce the need to repeatedly fetch data from main memory. In the end, the solution of the linear system is performed without the need to assemble the matrix A resulting from the bilinear form $a(\cdot,\cdot)$ (8). It is sufficient to pass the matrix-vector product operator to the Krylov solver. The solvers implemented in `NYMO` based on this principle are BICGSTAB [29] and GMRES [22].

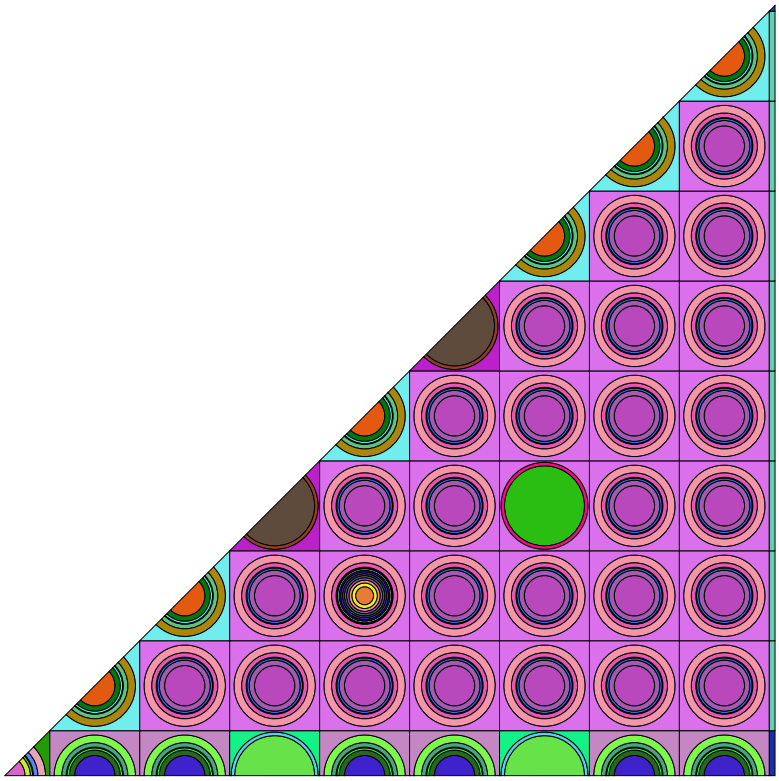

Figure 2: 312-cell mesh of an eighth PWR assembly. The elements of the same colors are equal up to a translation and thus belong to the same equivalence class. There are 49 classes, dividing the number of geometric matrices to be computed and stored by 6.

4 Applications

The numerical method described in the previous sections has been employed to solve to two 3D core calculation problems available in the literature. The first one is Takeda benchmark [25] and the second is the C5G7 benchmark [17]. These problems provide different configurations (10+3 in total), which offer a wide variety of geometries (cartesian, hexagonal, unstructured) with different optical properties, representative of FBR and PWR reactors. The simulations presented are eigenvalue calculations. The errors presented are relative error in pcm (1 pcm $= 10^{-5}$) regarding the reference solution (the Monte-Carlo solution provided by the benchmark authors)

$$e_r = \frac{\lambda_{approx} - \lambda_{ref}}{\lambda_{ref}}.$$

Two error criteria determine the convergence, one on the eigenvalue, the other on the fission source. The calculation stops when for two successive iterations, the variations on these two values are both below 10^{-5}. The linear solver used is GMRES [22], using the assembly-free framework described in section 3.5.

Pin power distributions presented in sections 4.2 and 4.3 are normalized such that the total power is equal to the number of fuel pins. To compare the pin power solution obtained to the reference distribution, three errors are calculated: the average (AVG), root mean square (RMS) and mean relative (MRE) pin power per cent error.

$$AVG = \frac{1}{N}\sum_{n=1}^{N}|e_n|\,, \quad RMS = \sqrt{\frac{1}{N}\sum_{n=1}^{N}|e_n^2|}, \quad MRE = \frac{1}{N\cdot p_{avg}}\sum_{n=1}^{N}|e_n|\cdot p_n. \tag{22}$$

The number of fuel pins is denoted N, p_n and e_n are respectively the reference value and the relative error in the nth fuel pin, p_{avg} is the reference average power.

All calculations are performed on a standard workstation housing two 12-core Intel® Xeon® Silver 4214 CPU at 2.20GHz.

4.1 Homogenised core calculation: Takeda Benchmark

The Takeda benchmark suite [25] comprises four different reactor models with two or three distinct cases per model, this amounts to 10 cases in total. All the calculations were performed using `NYMO` solver with P_4 order in angle and linear polynomial $\mathbb{P}^1$ in space. The reference Monte-Carlo solutions are taken from [25, p. 23]. For all calculated models, the relative errors compared to reference eigenvalue are below 40 pcm, with in particular one pcm obtained for case 2 of model 2. Models 1 and 2 eigenvalue calculation are performed in less than a minute. Here we give more details about the results obtained for problems 3 and 4, these being the most heterogeneous and time-consuming. Finally Figure 5 show the asymptotic behaviour of the k_{eff} according to the angular discretization.

4.1.1 Takeda model 3: cartesian geometry axially heterogeneous FBR

This model problem (Figure 3) is a Fast Breeder Reactor (FBR) core that has reflector and internal blanket region. There are three different cases depending on the material inserted in the control rod positions (rods or blanket cells). The core has 1/4 radial and 1/2 axial symmetry and the mesh elements used are of size Δx = Δy = Δz = 5 cm. We observe in Table 2 that the error is quite small (less than 38 pcm) with less than one minute calculation time.

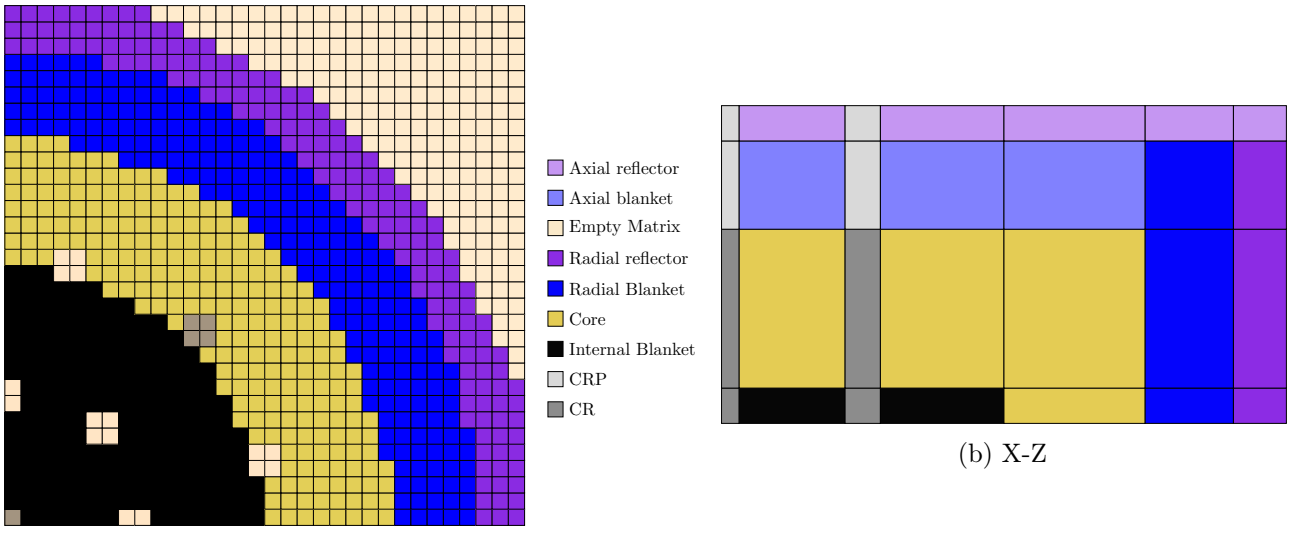

(a) X-Y

(b) X-Z

Figure 3: Takeda model 3, a cartesian geometry axially heterogeneous fast breeder reactor.

4.1.2 Takeda model 4: hexagonal geometry small FBR

This model (Figure 4) is a FBR core and has prismatic hexagonal geometry. Three cases with different control rod patterns are studied: withdrawn (case 1), half inserted (case 2) and fully inserted rods (case 3). For the mesh, all hexagons are divided into 24 (case 1) or 54 (case 2 and 3) equilateral triangles with $\Delta z = 5$ cm. Indeed, the presence of the control rods creates a discontinuity, and the mesh has been refined to take it into account. Table 2 shows that this allows us to obtain excellent results (less than 22 pcm) for all cases. Figure 5 shows the monotone convergence in angle, especially if we isolate odd and even orders. We go further into the convergence study in section 4.2.

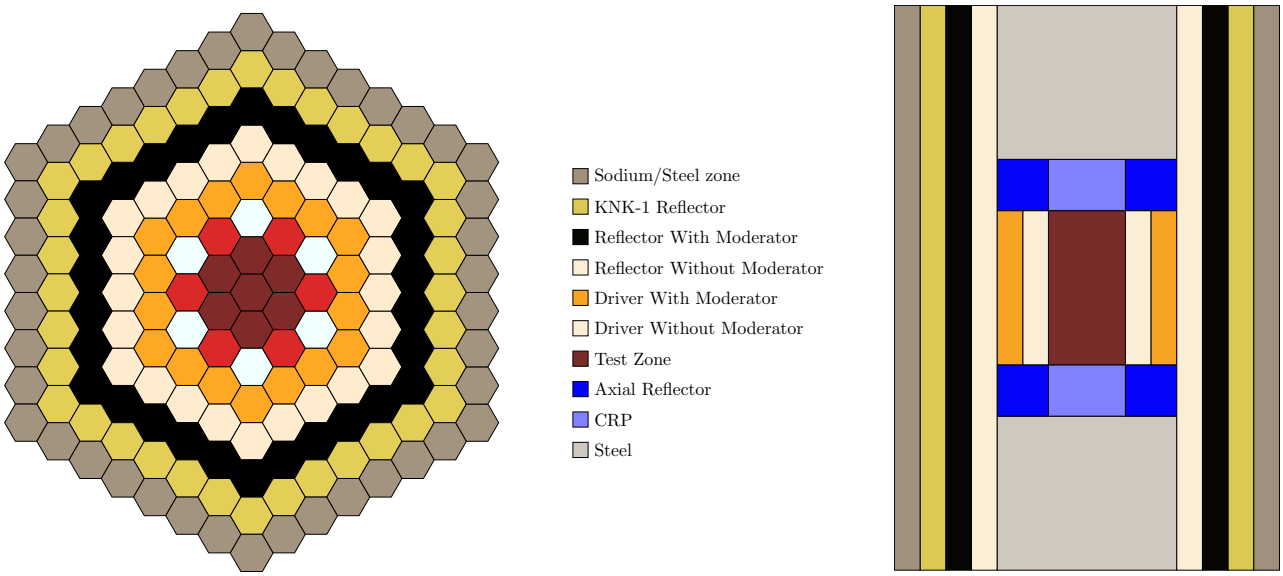

(a) X-Y (b) X-Z

Figure 4: Takeda model 4, an hexagonal geometry small fast breeder reactor.

Table 2: Relative error (pcm) and time (s) obtained with P_4 and $\mathbb{P}^1$ for Takeda models 3 and 4.

	Reference	NYMO	error	cpu time
Case 1	0.97090	0.97060	-30	49
Case 2	1.00050	1.00089	38	49
Case 3	1.02140	1.02147	6	51

(a) Model 3

	Reference	NYMO	error	cpu time
Case 1	1.09510	1.09521	10	474
Case 2	0.98330	0.98352	22	2636
Case 3	0.87990	0.87994	4	2349

(b) Model 4

4.2 Heterogeneous core calculation: 3D C5G7 Problem

The 3-D extended C5G7 MOx fuel assembly benchmark [17] is a problem designed to evaluate the ability of deterministic transport codes to handle reactor problems without spatial homogenization. It should be noted that in this benchmark, the cladding surrounding the fuel rod is smeared with the fuel pellet. The objectives are to calculate the effective multiplication factor and the normalized fission rate distributions (pin power) in three axial slices of the core.

4.2.1 Benchmark description and space-angular discretization

Figure 6a shows the radial configuration of this $128.52 \times 128.52 \times 128.52$ cm^3 small Pressurized Water Reactor (PWR) core, made up of four by four fuel assemblies, modeled in 1/4 radial symmetry and surrounded by a water reflector. Each assembly consists of a 17×17 lattice of square pin cells with the cell side equal to 1.26 cm. Fuel pins, control rods, guide tubes, and fission chambers are of circular shape with a 0.54 cm radius. The reflection boundary condition in zmin plane with inserted control rods makes the problem non-physical, which is explicitly

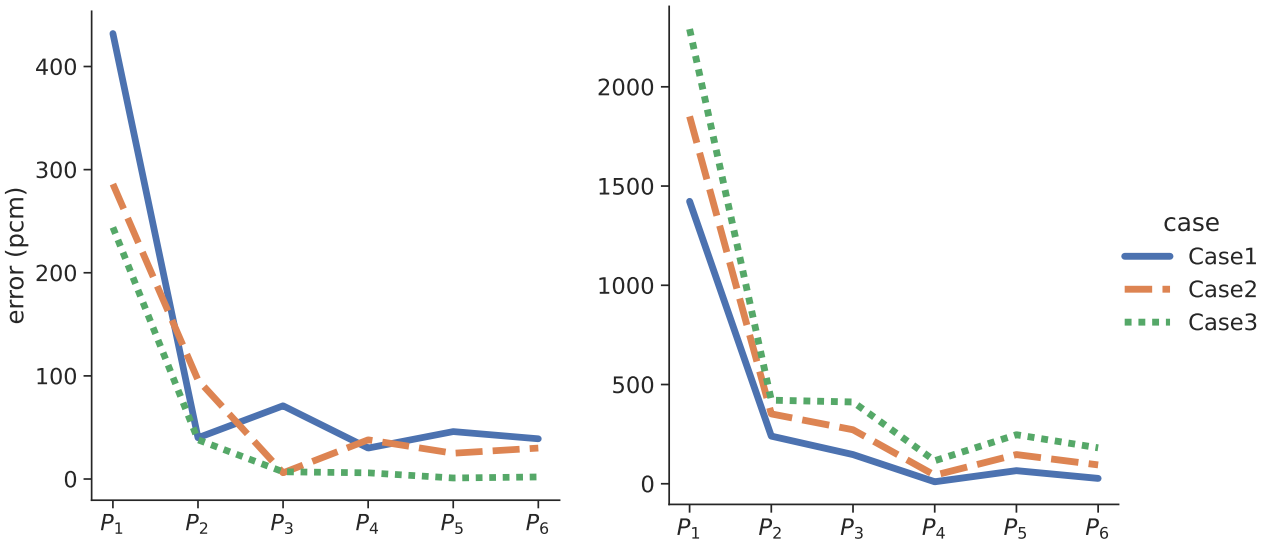

(a) Model 3

(b) Model 4

Figure 5: Convergence of the eigenvalue according to the angular discretization order.

stated in the problem description. Three problems (Unrodded, Rodded A and Rodded B) are considered to correspond to various levels of control rod insertion. The seven-group cross-sections with isotropic scattering for each material and detailed description are provided in [17].

For all calculation, the radial mesh used is described in Figure 6b. This radial mesh is the unique one applied to all calculations and it contains 15028 cells. Axial mesh has been varied starting from the coarsest one (denoted as Z_1) that has only one mesh interval within each fuel slice and reflector, and refining it progressively by subdividing these slices into two (Z_2), four (Z_4) and eight (Z_8) intervals. For polynomial discretization space, $\mathbb{P}^k$ refers to piecewise polynomial functions space of total degree at most k. That is, $\mathbb{P}^0$ the space of piecewise constant polynomial, $\mathbb{P}^1$ refers to space of piecewise linear polynomial and $\mathbb{P}^2$ refers to space of piecewise quadratic polynomial.

We performed a series of calculations by varying the $\mathrm{P_N}$ order from 1 to 6, the polynomial basis used are constant, linear and quadratic and the axial mesh refinement are 1, 2, 4 or 8. This involves 72 eigenvalue calculations for each test case. As before, each case was run on 24-core computer with an approximate computing time between 10 seconds (P_1, $\mathbb{P}^0$ without axial refinement) and 20 hours (P_6, $\mathbb{P}^2$, Z_8) for the most refined case.

4.2.2 Results of calculation and discussion

The first results show that, for all $\mathrm{P_N}$ orders, the error on the $\mathbb{P}^0$ polynomial space is high, so we discard these configurations from the further analysis. Moreover, the axial refinement does not seem to significantly improve the results. The differences between Z_4 and Z_8 refinements being very small (between 0 and 4 pcm) we excluded Z_8 from the rest of the analysis. Thus, we may conclude that the flux does not vary much axially and that it is not necessary to refine the mesh in this direction. This assumption is partially confirmed by [24], who studied the influence of the control rods by analysing the scalar fluxes along control rods. The authors observe that the axial scalar fluxes decreases in the vicinity of the reflector, but vary little in each slice in MOx and UOx outer assemblies. Moreover, the flux variation is more pronounced in the UOx inner assembly when the control rods are inserted (Rodded A and B). In our case, for Rodded A, the best results are still obtained without refinement, while Rodded B gives better results by subdividing each z-slice in two. Tables 3, 4 and 5 present for each case, the k_{eff} obtained with one low-order and one high-order discretization. For the Unrodded and Rodded A cases, the best results are respectively 13 pcm and -29 pcm and obtained with P_5 $\mathbb{P}^2$, while for Rodded B the best solution have 6 pcm error and obtained with P_6 $\mathbb{P}^1$. Considering only the configurations running in less than 3 min (180s) the best result is -48 pcm (P_1 $\mathbb{P}^2$ Z_1) for Unrodded, -80 pcm for Rodded A and -162 pcm Rodded B (the two with P_2 $\mathbb{P}^1$ Z_1).

Figure 7 shows the variation of eigenvalue relative error according to $\mathrm{P_N}$ order for each of the polynomial spaces $\mathbb{P}^1$ and $\mathbb{P}^2$. In all three cases, the results are presented for Z_2 refinement. We make several observations here. First, for all polynomial spaces, separating the even (green lines) and odd (red lines) $\mathrm{P_N}$ orders, we observe a monotone convergence. In the first two cases however, the even $\mathrm{P_N}$ orders stagnate or increase slightly. This

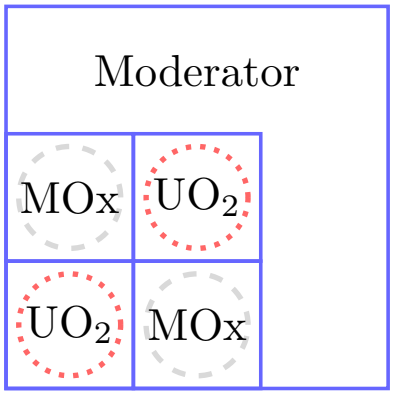

(a) X-Y Geometry

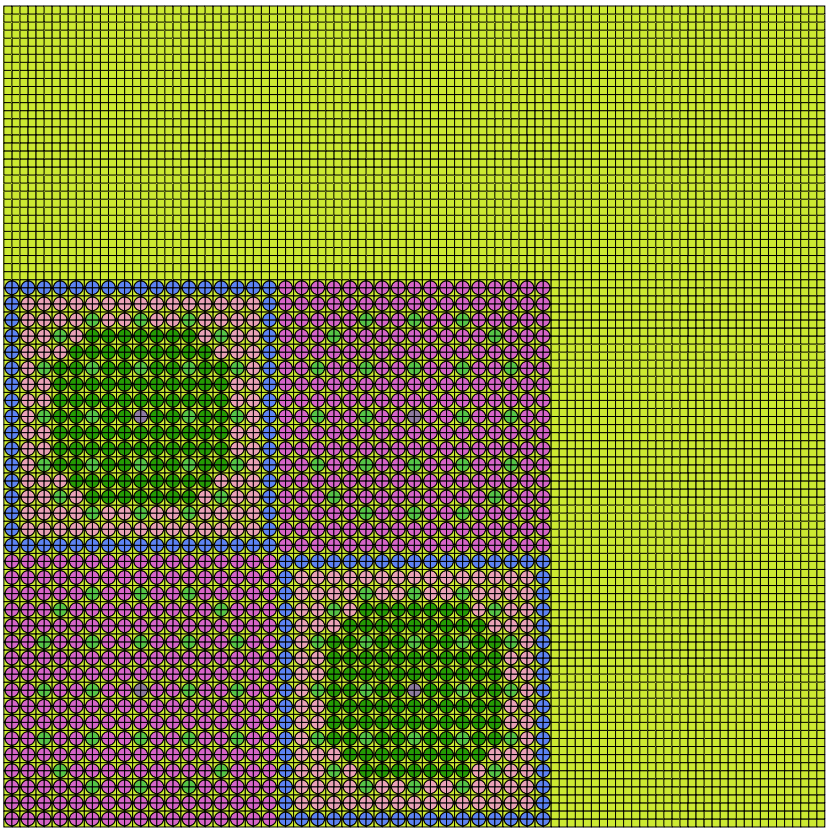

(b) Radial mesh used for calculations.

Figure 6: C5G7 quarter core radial geometry configuration and mesh used for calculations.

Table 3: Eigenvalue error for Unrodded case of C5G7 problem without axial refinement (Z_1).

Unrodded	k_{eff}	error (pcm)	time (s)
MCNP	1.14308	± 6	-
P_1 $\mathbb{P}^2$	1.14253	-48	157
P_5 $\mathbb{P}^2$	1.14324	13	5191

Table 4: Eigenvalue error for Rodded A case of C5G7 problem without axial refinement (Z_1).

Rodded A	k_{eff}	error (pcm)	time (s)
MCNP	1.12806	± 6	-
P_2 $\mathbb{P}^1$	1.12715	-80	142
P_5 $\mathbb{P}^2$	1.12773	-29	5389

Table 5: Eigenvalue error for Rodded B case of C5G7 problem, each axial slice is divided by two (Z_2).

Rodded B	k_{eff}	error (pcm)	time (s)
MCNP	1.07777	± 6	-
P_2 $\mathbb{P}^1$	1.07894	108	322
P_6 $\mathbb{P}^1$	1.07784	6	6084

behaviour is for the moment unexplained. Second, for even (resp. odd) P_N the error obtained is smaller in polynomial space $\mathbb{P}^1$ (resp. $\mathbb{P}^2$). And finally, we note that the even (resp. odd) P_N converge to the reference solution by overestimating (resp. underestimating) it. This oscillatory approach to the asymptotic regime, but monotonous if one takes separately odd and even orders, has already been observed in previous works on the 2D solutions, in [4] on reactivity and in [27] on the flux shape. In the latter, a different finite element approximation is used, which may suggest that this behavior is due to the properties of spherical harmonic approximation itself, but for the moment it remains unexplained. All these observations deserve further investigation.

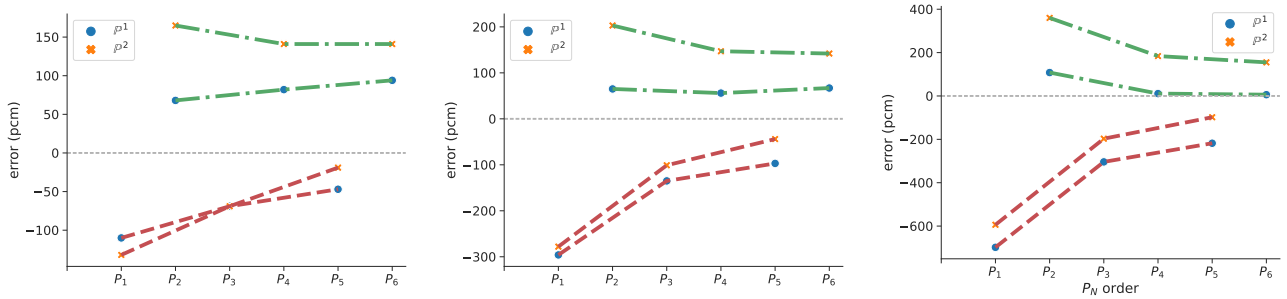

(a) Unrodded (b) Rodded A (c) Rodded B

Figure 7: 3D-C5G7 $k-$eigenvalue relative error in pcm according to the angular-space discretization. Even (resp. odd) P_N orders are connected by green (resp. red) dotted lines.

We next proceed to the pin power calculations with the configurations that provide the best multiplication factor of each case. Table 6 shows the error made at maximum pin power, the average (AVG), root mean square (RMS) and mean relative (MRE) errors on the pin power distribution (defined in [17, p. 25]). The calculations are performed with P_5 $\mathbb{P}^2$ Z_1 for the first two cases and P_6 $\mathbb{P}^1$ Z_2 for Rodded B. For the first two cases, the calculations exhibit errors less than 0.6% compared to the MCNP solution. We obtain a slightly bigger error (less than 1%) on the last case because of strong discontinuities introduced by control rods insertion. In overall, these results comply well with the reference values.

Table 6: Pin power distribution metrics for C5G7 benchmark problem.

Benchmark case		Unrodded	Rodded A	Rodded B
Pin power error (%)	Max Rate	-0.084	-0.398	-1.221
	AVG	0.225	0.301	0.743
	RMS	0.280	0.398	0.835
	MRE	0.171	0.249	0.764
Assembly power error (%)	UOx Inner	0.014	-0.178	-0.980
	MOx	-0.135	0.041	0.476
	UOx Outer	0.365	0.662	0.866

4.3 Lattice Calculation: 281-groups PWR UOx Fuel Assembly

This section is devoted to eigenvalue and pin power distribution calculation a 2D PWR UO_2 Fuel Assembly described in [30, §III. 1]. It is a typical 17×17 pin assembly motif containing UO_2 and gadolinium fuel rods and guide tubes. The aim of this study is to present a realistic test case with 281 energy groups taking into account anisotropic scattering. The results obtained are compared with deterministic solvers, here `TDT` [11], the `APOLLO3`® characteristics method (MOC) and `IDT` [19, 18, 2] the method of short characteristics.

4.3.1 Case description and discretization

Figure 8 shows a schematic view of the UO_2 fuel assembly geometry. Due to symmetries, it is sufficient to represent one-eighth of the structure. Each pin cell is modelled without homogenization, the thickness of cladding being 0.064 cm. In this study, the original UO_2 properties are replaced with 4.2% enriched fuel with isotopic

composition given in Table 7. The order of anisotropy is 3, and a self-shielding calculation is performed first to obtain 281-groups cross-sections.

The mesh used for this experiment is displayed in Figure 9. The fuel pin is subdivided in six concentric annuli while the gadolinium bearing fuel is subdivided into eleven, accounting for spatially dependent self-shielding effect and preparing the model for depletion calculation. For `NYMO`, P_5 angular approximation and constant $\mathbb{P}^0$ spatial discretization yield to 16 million of degrees of freedom. The step-constant MOC (`TDT`) is used with 30 azimuthal angles and 12 polar angles. The `IDT` solver is used with a classical S_8 level symmetric quadrature and linear characteristic option.

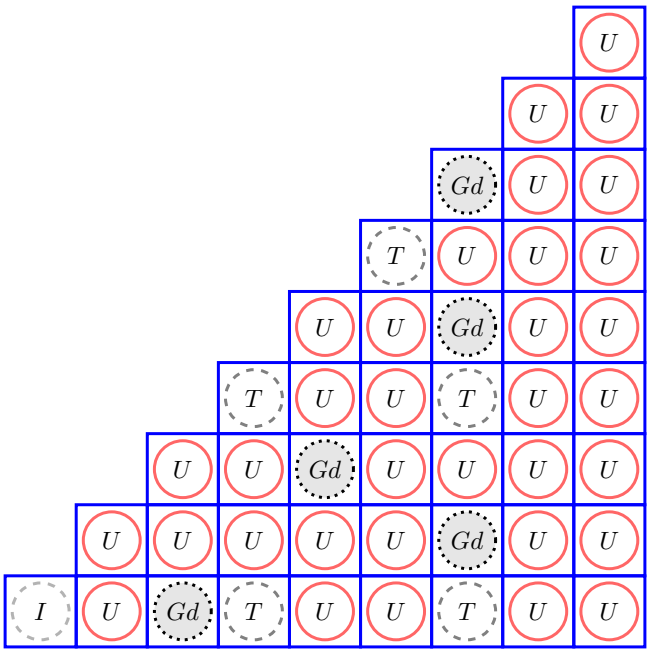

Figure 8: PWR UO_2 fuel assembly 1/8th geometry layout, with UO2 fuel rod (U), gadolinium pins (Gd), RCC guide thimble (T) and instrumentation thimble (I).

Table 7: UOX fuel composition.

Isotope	Atomic number density (#/barn/cm)
U234	4.6498E-07
U235	9.7229E-04
U236	2.3051E-07
U238	2.1874E-02
O16	4.5693E-02

4.3.2 Results and discussions

Table 8 presents eigenvalue, computation time and overall pin power distribution error when comparing `NYMO` to `TDT` and `IDT`. A k_{eff} of 0.999568 have been obtained, 121 pcm above the `TDT` solution. The 400 pcm spread compared to `IDT` is due to the absence of ring sectors in `IDT` calculations. To conclude the analysis, the pin power distributions are compared. The pin power solutions (Figure 10) are normalized such that the total power is equal to the number of fuel pins (264). As shown in Figure 11, the `NYMO` normalized pin power are all within 1 % of the `TDT` results and are less than 1.47 % regarding `IDT`.

The nature of the two approximations being very different, this results is considered to be very satisfactory.

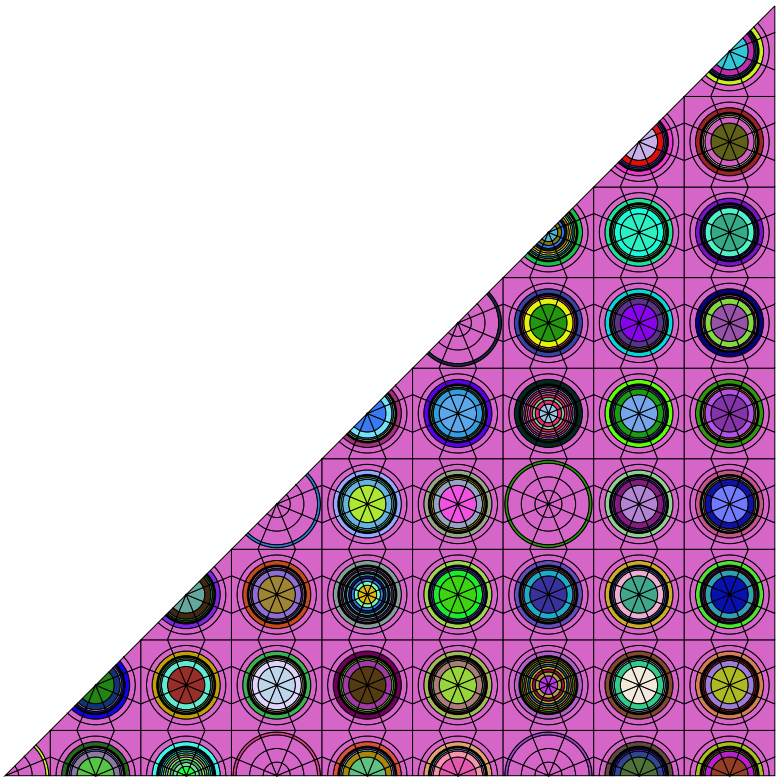

Figure 9: Mesh used for PWR UO_2 Fuel Assembly Calculation.

Table 8: `NYMO` eigenvalue and power map compared to `TDT` and `IDT` for the PWR UO_2 assembly.

	`NYMO`	`TDT`	`IDT`
k_{eff}	0.999568	0.998360	0.995493
Δk_{eff} (pcm)	-	121	407
Max (%)	-	0.794	1.468
AVG (%)	-	0.314	0.461
RMS (%)	-	0.384	0.607
MRE (%)	-	0.295	0.381
time (s)	142	176	-

5 Conclusion

The implementation of the three-dimensional extension of the previously developed discontinuous Galerkin P_N method has been described and its capabilities illustrated on the examples of the well-known Takeda and C5G7 benchmarks. The discretization method is able to handle the mesh elements of different shapes, in general arbitrary, but in practical applications all geometries describing the fuel elements without any simplification nor homogenisation. The presented results show that the method is able to attain an accuracy better than 100 pcm in reactivity for a computation time less than 10 minutes on a desktop machine. The investigated cases show an error smaller than 30 pcm and in some of these of order of one pcm.

Moreover, tests have been conducted on a realistic of PWR assembly in 281 energy groups with anisotropic scattering, and the obtained results agreed well with other, characteristic-based transport solvers.

The convergence behaviour of odd and even order expansions are different and need further theoretical analysis. Nevertheless, the method seems to be consistent and stable showing competitive computational times, and it opens the way to its application to high fidelity simulations of a whole core. Obviously, this approach needs an implementation of a distributed memory parallel algorithm. Current work focused on convergence analysis of the method and distributed memory parallelization.

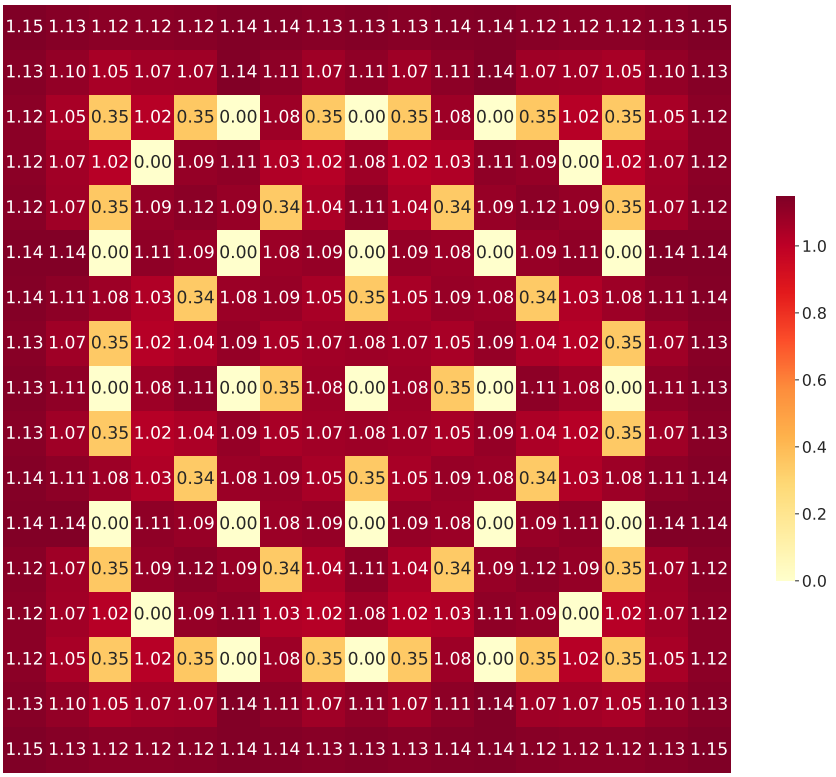

Figure 10: NYMO normalized power distribution for the PWR UO_2 fuel assembly.

Acknowledgments

K. Assogba's PhD research work is supported by the CEA NUMERICS program, which has received funding from the European Union's Horizon 2020 research and innovation program under the Marie Sklodowska-Curie grant agreement No 800945.

References

[1] K. Assogba, L. Bourhrara, I. Zmijarevic, and G. Allaire. Precise 3D Reactor Core Calculation Using Spherical Harmonics and Discontinuous Galerkin Finite Element Methods. In *Proceedings of International Conference on Physics of Reactors 2022 (PHYSOR 2022)*, pages 1224–1233, Pittsburgh, PA, United States, May 2022. American Nuclear Society.

[2] Y. S. Ban, E. Masiello, R. Lenain, H. G. Joo, and R. Sanchez. Code-to-code comparisons on spatial solution capabilities and performances between nTRACER and the standalone IDT solver of APOLLO3®. *Annals of Nuclear Energy*, 115:573–594, May 2018.

[3] L. Bourhrara. New Variational Formulations for the Neutron Transport Equation. *Transport Theory and Statistical Physics*, 33(2):93–124, January 2004.

[4] L. Bourhrara. A new numerical method for solving the Boltzmann transport equation using the PN method and the discontinuous finite elements on unstructured and curved meshes. *Journal of Computational Physics*, 397, July 2019.

[5] F. Brezzi, L. D. Marini, and E. Süli. Discontinuous galerkin methods for first-order hyperbolic problems. *Mathematical Models and Methods in Applied Sciences*, 14(12):1893–1903, December 2004.

[6] S. Chandrasekhar. On the Radiative Equilibrium of a Stellar Atmosphere. II. *The Astrophysical Journal*, 100:76, 1944.

[7] R. Dautray and J.-L. Lions. *Mathematical Analysis and Numerical Methods for Science and Technology*, volume 6. Springer Berlin Heidelberg, Berlin, Heidelberg, 1988.

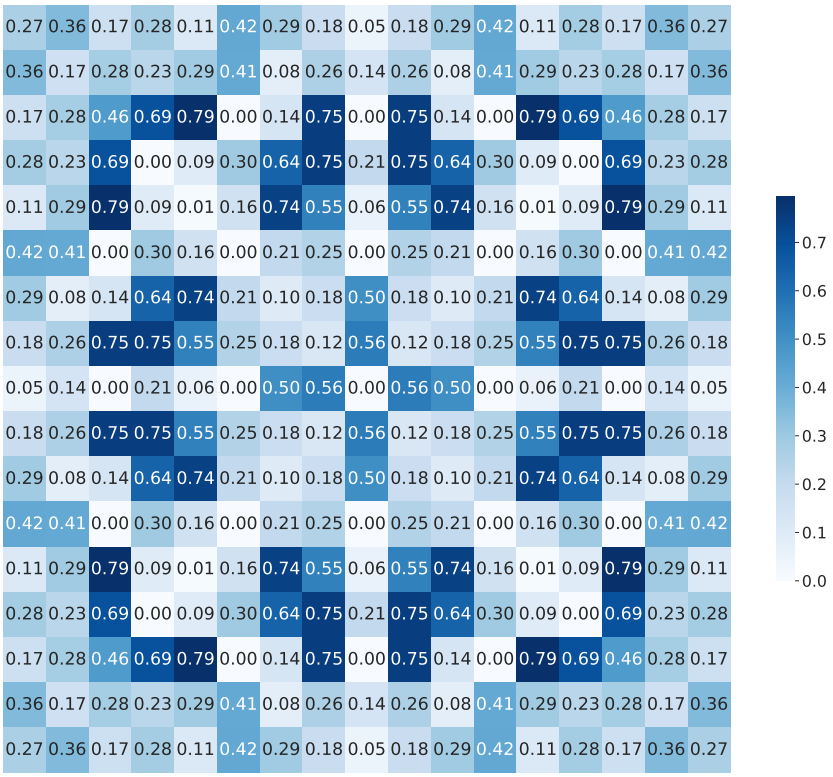

(a) NYMO compared to TDT.

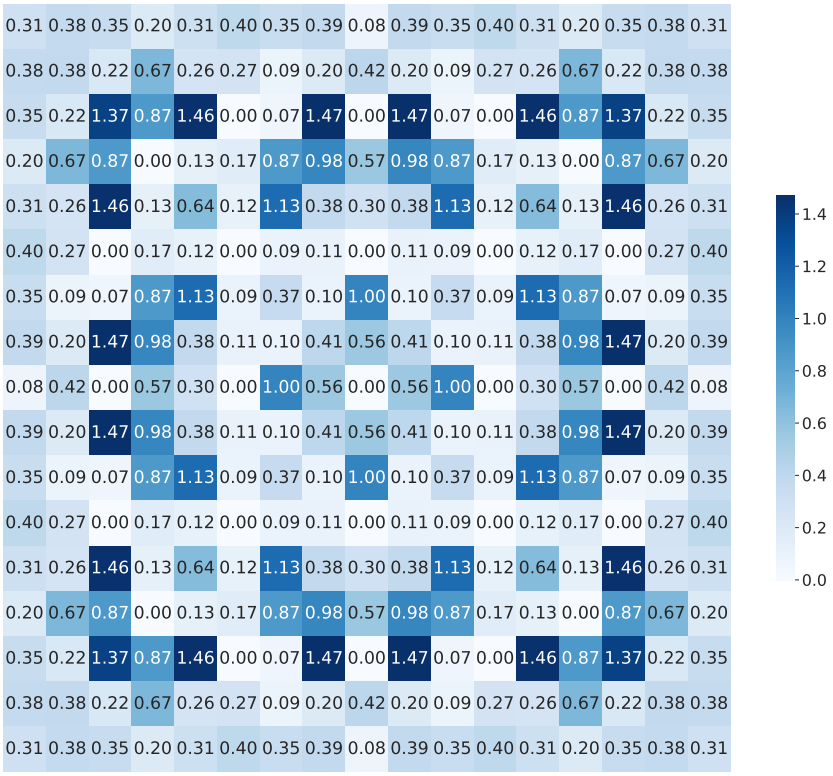

(b) NYMO compared to IDT.

Figure 11: NYMO power distribution absolute relative error (in %) related to TDT (top) and IDT (bottom).

[8] B. Davison. Spherical-harmonics method for neutron transport theory problems with incomplete symmetry. *Canadian Journal of Physics*, 36(4):462–475, April 1958.

[9] C. R. E. de Oliveira. An arbitrary geometry finite element method for multigroup neutron transport with anisotropic scattering. *Progress in Nuclear Energy*, 18(1):227–236, January 1986.

[10] J. Duderstadt and W. Martin. *Transport Theory*. John Wiley and Sons, New York, 1979.

[11] A. Gammicchia, S. Santandrea, and S. Dulla. Cross sections polynomial axial expansion within the APOLLO3® 3D characteristics method. *Annals of Nuclear Energy*, 165:108673, January 2022.

[12] C. Johnson and J. Pitkäranta. An analysis of the discontinuous Galerkin method for a scalar hyperbolic equation. *Mathematics of Computation*, 46(173):1–26, 1986.

[13] K. D. Lathrop. Ray Effects in Discrete Ordinates Equations. *Nuclear Science and Engineering*, 32(3):357–369, June 1968.

[14] P. Lesaint and P. A. Raviart. On a Finite Element Method for Solving the Neutron Transport Equation. In C. de Boor, editor, *Mathematical Aspects of Finite Elements in Partial Differential Equations*, pages 89–123. Academic Press, January 1974.

[15] E. E. Lewis, C. B. Carrico, and G. Palmiotti. Variational Nodal Formulation for the Spherical Harmonics Equations. *Nuclear Science and Engineering*, 122(2):194–203, February 1996.

[16] E. E. Lewis and W. F. Miller. *Computational Methods of Neutron Transport*. Wiley, New York, 1984.

[17] E. E. Lewis, G. Palmiotti, T. A. Taiwo, R. N. Blomquist, M. A. Smith, and N. Tsoulfanidis. Benchmark specifications for deterministic MOX fuel assembly transport calculations without spatial homogenization (3-D extension C5G7 MOX). *Organization for Economic Co-operation and Development's Nuclear Energy Agency*, OECD/NEA document, NEA/NSC/DOC(2003)6, 2003.

[18] E. Masiello, R. Lenain, and W. Ford. 3D heterogeneous Cartesian cells for transport-based core simulations. *Annals of Nuclear Energy*, 142:107364, July 2020.

[19] E. Masiello, R. Sanchez, and I. Zmijarevic. New Numerical Solution with the Method of Short Characteristics for 2-D Heterogeneous Cartesian Cells in the APOLLO2 Code: Numerical Analysis and Tests. *Nuclear Science and Engineering*, 161(3):257–278, March 2009.

[20] J. E. Morel and J. M. McGhee. A Self-Adjoint Angular Flux Equation. *Nuclear Science and Engineering*, 132(3):312–325, July 1999.

[21] W. Reed and T. Hill. Triangular mesh methods for the neutron transport equation. Technical Report LA-UR-73-479, Los Alamos Scientific Laboratory, United States, 1973.

[22] Y. Saad and M. H. Schultz. GMRES: A Generalized Minimal Residual Algorithm for Solving Nonsymmetric Linear Systems. *SIAM Journal on Scientific and Statistical Computing*, 7(3):856–869, July 1986.

[23] D. Schneider, F. Dolci, F. Gabriel, J.-M. Palau, M. Guillo, and B. Pothet. APOLLO3® CEA/DEN deterministic multi-purpose code for reactor physics analysis. In *PHYSOR 2016 – Unifying Theory and Experiments in the 21st Century*, Sun Valley, United States, May 2016.

[24] A. Seubert, W. Zwermann, and S. Langenbuch. Solution of the C5G7 3-D extension benchmark by the SN code TORT. *Progress in Nuclear Energy*, 48(5):432–438, July 2006.

[25] T. Takeda and H. Ikeda. 3-D Neutron Transport Benchmarks. *Journal of Nuclear Science and Technology*, 28(7):656–669, 1991.

[26] D. Tomatis, F. Bidault, A. Bruneton, and Z. Stankovski. Overview of SERMA's Graphical User Interfaces for Lattice Transport Calculations. *Energies*, 15(4):1417, January 2022.

[27] S. Van Criekingen, E. E. Lewis, and R. Beauwens. Mixed-Hybrid Transport Discretization Using Even and Odd PN Expansions. *Nuclear Science and Engineering*, 152(2):149–163, February 2006.

[28] S. Van Criekingen, F. Nataf, and P. Havé. Parafish: A parallel FE–PN neutron transport solver based on domain decomposition. *Annals of Nuclear Energy*, 38(1):145–150, January 2011.

[29] H. A. van der Vorst. Bi-CGSTAB: A Fast and Smoothly Converging Variant of Bi-CG for the Solution of Nonsymmetric Linear Systems. *SIAM Journal on Scientific and Statistical Computing*, 13(2):631–644, March 1992.

[30] A. Yamamoto, T. Ikehara, T. Ito, and E. Saji. Benchmark Problem Suite for Reactor Physics Study of LWR Next Generation Fuels. *Journal of Nuclear Science and Technology*, 39(8):900–912, August 2002.